THE JOURNAL OF
PHYSICAL CHEMISTRY C

Article

Cite This: J. Phys. Chem. C 2019, 123, 19649−19658

pubs.acs.org/JPCC

Effect of Surface Hydrophilicity on the Interfacial Properties of a Model Octane−Water−Silica System

Wenjing Guo and Jeffrey R. Errington*

Department of Chemical and Biological Engineering, University at Buffalo, Buffalo, New York 14260-4200, United States

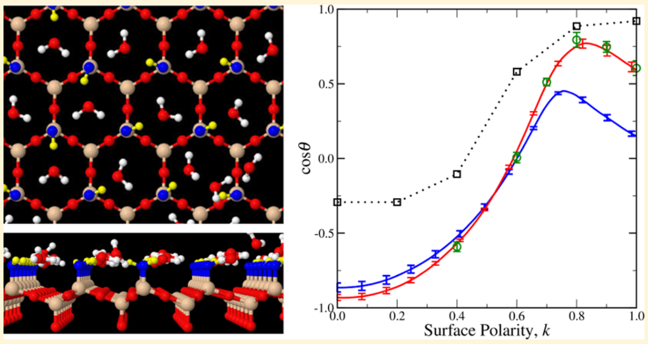

ABSTRACT: We use molecular simulation to study the impact of substrate hydrophilicity on the wetting properties of water at a hydroxylated β-cristobalite (111) surface in a mother *n*-octane liquid. We employ the silica model introduced by Lee and Rossky [Lee, S. H.; Rossky, P. J. *J. Chem. Phys.* **1994**, *100*, 3334−3345]. The hydrophilicity of the substrate is tuned by scaling the magnitude of partial charges placed on atoms within the first layer of the silica substrate (modification of the substrate polarity). An interface potential approach is used to compute the contact angle of a water droplet at the substrate over a wide range of hydrophilicities at temperatures of 300 and 400 K. Our results illustrate an anomalous trend in the contact angle of water. For relatively hydrophobic surfaces, the system behaves as is expected, with increases in substrate polarity resulting in a decrease in the contact angle. However, at a sufficiently high substrate polarity, the value of the contact angle reaches a minimum, with further increases in polarity leading to an increase in the contact angle. The amount of water adsorbed at the interface changes abruptly in the vicinity of the extremum point. From a macroscopic perspective, a monolayer-thick precursor film surrounds the droplet at sufficiently high substrate polarity. We link the evolution of these macroscopic properties to the manner in which water organizes at the β-cristobalite (111) surface. The structure is characterized via analysis of configurational snapshots, density profiles, in-plane radial distribution functions, and molecular orientation probability distributions. The analysis reveals that water molecules reside within the hollows of the β-cristobalite (111) surface at sufficiently high substrate polarity. As the polarity increases, the interfacial water molecules progressively adopt a more planar structure and limit the number of hydrogen bonds that they form with water in subsequent interfacial layers. This evolution of the interfacial water structure leads to an effective weakening of the water−substrate interaction and corresponding increase in the water contact angle.

INTRODUCTION

The wetting behavior of fluids containing hydrocarbon and water on solid surfaces has been the subject of many investigations because of its relevance in numerous chemical processes and technologies. In the oil industry, the wetting behavior of hydrocarbon−water−rock systems plays an important role in the design of enhanced oil recovery (EOR) processes. The wettability of the rock surface and the interfacial tension of the water−hydrocarbon interface influence how water and oil distribute within rock pores.[1,2] In a water-wet reservoir, water preferentially adsorbs at the rock surface, and oil is easily displaced by water in waterflooding processes. In contrast, oil preferentially adsorbs at the rock surface in oil-wet reservoirs, thus inhibiting the mobility of the oil phase. Therefore, many EOR methods rely on altering the wettability of the mineral from oil wetting to preferentially water wetting.[3] The wettability of a reservoir is strongly influenced by the surface chemistry/structure of the minerals (rock) as well as fluid composition, temperature, and pressure. In previous work, we examined the wetting properties of a model water−hydrocarbon−mineral system over a wide range of thermodynamic variables (temperature, pressure, and fluid composition). In this work, we study the effect of surface chemistry (hydrophilicity) on the wetting behavior.

The effect of substrate strength on interfacial properties has been examined by our group[4−8] and several others.[9−14] These molecular simulation studies have shown that the contact angle of the solid−fluid system generally decreases with increasing substrate strength. At sufficiently high substrate strength, the system reaches a wetting point, and the fluid spreads evenly at the surface. For example, we considered the Lennard-Jones fluid at both structureless and atomistically detailed surfaces and found that the contact angle monotonically decreases with increasing substrate strength over a wide range of temperature.[5,6] For relatively weak surfaces, the rate of change of the cosine of the contact angle increases with increasing substrate strength. As the system approaches the wetting point, the cosine of the contact angle is generally near linear in substrate strength.[6] In a later study, our group considered water at three model nonpolar surfaces (graphite, fcc solid, and structure-

Received: May 25, 2019
Revised: July 5, 2019
Published: July 8, 2019

DOI: 10.1021/acs.jpcc.9b04970
J. Phys. Chem. C 2019, 123, 19649−19658

less).[8] These systems showed the same qualitative trends as the Lennard-Jones systems. We also found that the contact angle data nearly collapsed onto a common curve when plotting with a scaled surface strength, suggesting that the structure of the surface had a relatively little impact on the evolution of the contact angle with substrate strength. Finally, we note that all of the systems exhibited similar temperature dependence of the contact angle.[6−8] For sufficiently weak surfaces, the contact angle increases with increasing temperature. In contrast, for surfaces of moderate to strong strength, the contact angle decreases with increasing temperature.

Giovambattista et al. considered the wetting behavior of water at a model hydroxylated silica substrate with variable hydrophilicity.[9] More specifically, they considered how the contact angle of a water nanodroplet and the structure of water in the vicinity of the surface change with hydrophilicity. The hydrophilicity of the surface was tuned by scaling the partial atomic charges within the first silica layer, thus modifying the polarity of the substrate. The group found that the contact angle monotonically decreased with increasing hydrophilicity. The system remained within the partial wetting regime over the range of polarities studied. This trend is qualitatively consistent with those exhibited by the systems with nonpolar substrates noted above, that is, the contact angle decreases as the strength of the surface−fluid interaction increases. The contact angle also coupled closely to the water orientation probability distribution. The preferred direction of the oxygen−hydrogen water bonds relative to the surface normally evolved continuously with substrate hydrophilicity.[9]

In this work, we are interested in understanding the impact of substrate polarity on the water contact angle for a water−hydrocarbon mixture at a silica interface. We adopt the water model and silica substrate and mean to tune the surface hydrophilicity considered by Giovambattista and co-workers.[9] In contrast, we take the mother background phase to be a hydrocarbon liquid (*n*-octane). We also employ a different collection of methods to compute interfacial properties of interest. Giovambattista et al. utilized a nanodroplet technique[15−17] to evaluate the contact angle. Here, we use the interface potential approach[4,6,7,18−22] to calculate the contact angle of water over a wide range of substrate conditions.

We recently introduced an interface potential-based approach for computing the wetting properties of water−hydrocarbon−mineral systems.[22,23] We used a combination of direct simulations, which capture the complete interface potential at a specified state and substrate condition, and expanded ensemble simulations, which provide the variation in interfacial properties over a range of state and substrate conditions, to evaluate properties of interest. Two interface potentials are considered. The first focuses on the surface excess free energy associated with the growth of a water film from a mineral substrate in a mother hydrocarbon fluid. The second focuses on the surface excess free energy associated with the growth of a hydrocarbon film from a mineral substrate in a mother aqueous liquid. Together, these potentials enable one to deduce the water contact angle and water−hydrocarbon interfacial tension. The local structure of water in the vicinity of the silica surface also features prominently in our study. A number of structural metrics are used to analyze the fluid structure. Specifically, we characterize the structure of water near the silica surface via density profiles, in-plane radial distribution functions, and molecular orientation probability distribution functions.

Our results reveal an interesting wetting behavior. At sufficiently high substrate hydrophilicity, the water contact angle reaches a minimum. At relatively low hydrophilicity, the system shows the expected behavior, with an increase in substrate polarity resulting in a decrease in the contact angle. However, as the system approaches the wetting point, the contact angle reaches an extremum, with further increases in substrate polarity resulting in an increase in the contact angle. We link this extremum to the manner in which water organizes at the silica surface. When the silica−water interaction becomes sufficiently strong, water molecules preferentially sit at regular positions defined by the topography of the silica surface. The surface density of water increases rapidly around this point. From a macroscopic perspective, a monolayer-thick precursor film forms in the vicinity of the droplet. We use molecular simulation to explore connections between macroscopic interfacial properties and the microscopic fluid structure at the interface.

We note that observations of water organizing into regular patterns at mineral surfaces have been reported in previous studies.[24,25] Various structures have been observed, including isolated monomers, clusters, one-dimensional chains, and two-dimensional films. Yang et al. used density functional theory to study how water organizes in the vicinity of the (100) and (111) surfaces of hydroxylated cristobalite.[26] They found that water forms distinct patterns at these two substrates. For the β-cristobalite (110) surface, water sits above the substrate and forms a hydrogen bond network wherein water forms bonds between both the silica substrate and adjacent water molecules. For the β-cristobalite (111) surface, isolated water molecules sit on the hollow sites of the underlying substrate. Water molecules are separated by nearly 5 Å and the hydrogen bond with the silica substrate only. We study the β-cristobalite (111) surface here and observe water patterns that are consistent with the Yang et al. study.[26] In this work, the formation of these patterns is related to changes in the macroscopic wetting behavior.

This article is organized as follows. In the following section, we describe the molecular models and simulation methods used in this work. Next, we present our simulation results for macroscopic wetting properties and show how these are related to structural metrics that related to how water organizes at the interface. Finally, we provide concluding remarks.

■ MOLECULAR MODEL AND METHODS

Methods. We employ an interface potential-based approach[27−29] to study the wetting properties of the octane−water mixture at a silica surface. Detailed information related to this approach is available in earlier reports from our group.[4,6−8,20−22,30] We work with two variants of the interface potential. The water spreading interface potential $W^{\mathrm{w,os}}(l^{\mathrm{w}})$ provides the surface excess free energy associated with the growth of a water-rich film of thickness l^{w} from the silica surface in a mother octane-rich liquid. Examples of $W^{\mathrm{w,os}}(l^{\mathrm{w}})$ are provided in Figure 2 of ref 22 (see also Figure 1 below). The octane spreading interface potential $W^{\mathrm{o,ws}}(l^{\mathrm{o}})$ provides the surface excess free energy associated with the growth of an octane-rich film of thickness l^{o} from the silica surface in a mother water-rich liquid. Examples of $W^{\mathrm{o,ws}}(l^{\mathrm{o}})$ are provided in Figure 3 of ref 22. For partial wetting conditions, the water and octane spreading coefficients, $s^{\mathrm{w,os}}$ and $s^{\mathrm{o,ws}}$ are obtained from

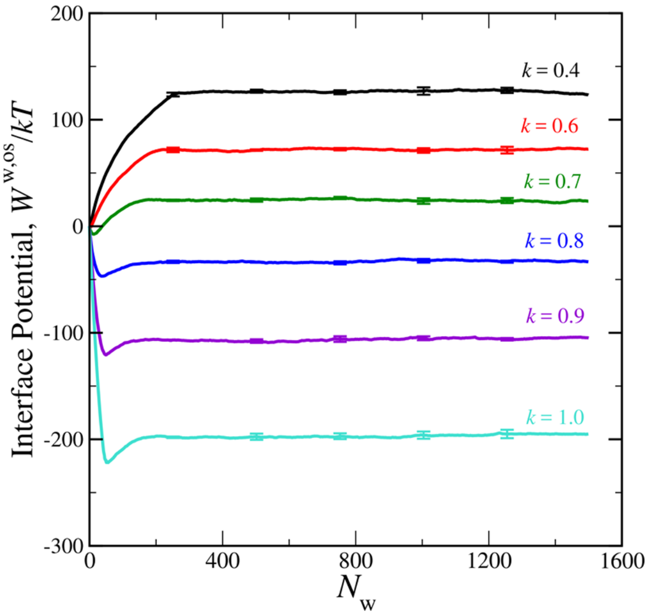

Figure 1. Water spreading interface potential at select surface polarities.

an analysis of the water and octane interface potentials, respectively. More specifically, $s^{\mathrm{w,os}}$ and $s^{\mathrm{o,ws}}$ are given by the difference in the minimum and plateau regions of the relevant interface potential. These spreading coefficients are used to determine the water−octane interfacial tension, $2\gamma^{\mathrm{ow}} = -(s^{\mathrm{w,os}} + s^{\mathrm{o,ws}})$ and the contact angle θ of a water-rich droplet at a silica substrate in a mother octane-rich fluid, $2\gamma^{\mathrm{ow}} \cos\theta = s^{\mathrm{w,os}} - s^{\mathrm{o,ws}}$.

A two-step approach is used to obtain γ^{ow} and θ over a wide range of state conditions and/or substrate characteristics. In the first step, direct calculations are conducted to compute $W^{\mathrm{w,os}}(l^{\mathrm{w}})$ and $W^{\mathrm{o,ws}}(l^{\mathrm{o}})$ curves at select conditions from which we extract absolute values of $s^{\mathrm{w,os}}$ and $s^{\mathrm{o,ws}}$, respectively. Independent expanded ensemble calculations[22,31,32] are then used to determine how the free energies of the minimum and plateau regions of the interface potential vary along a path of interest. The results of these calculations are combined to obtain the variation in a spreading coefficient ($s^{\mathrm{w,os}}$ or $s^{\mathrm{o,ws}}$) along the path. Finally, the relative spreading coefficient curve is connected to a known absolute value of the spreading coefficient at a given point. Once $s^{\mathrm{w,os}}$ and $s^{\mathrm{o,ws}}$ are known along the path of interest, γ^{ow} and θ readily follow.

In our previous study,[22] we obtained $s^{\mathrm{w,os}}$, $s^{\mathrm{o,ws}}$, γ^{ow}, and θ over a wide range of temperatures and pressures at two values of the substrate polarity. In this work, we are interested on how interfacial properties vary with substrate polarity at two state conditions. Specifically, we complete calculations at $T = 300$ K and $p = 10$ MPa and $T = 400$ K and $p = 10$ MPa. An expanded ensemble approach is employed to determine the variation in the wetting properties with substrate polarity as outlined above. Results from our previous study provide the necessary reference data.

Model. We work with the united atom TraPPE model for octane,[33] the SPC/E model for water,[34] and the Lee and Rossky model for silica.[35] The energy of interaction $u(r)$ between two interaction sites separated by four or more bonds and by a distance r is given by the potential

$$u(r) = 4\varepsilon_{ij}\left[\left(\frac{\sigma_{ij}}{r}\right)^{12} - \left(\frac{\sigma_{ij}}{r}\right)^{6}\right]S(r) + \frac{1}{4\pi\varepsilon_{\mathrm{o}}}\frac{q_i q_j}{r} \tag{1}$$

with

$$S(r) = \begin{cases} 1 & r < r_{\mathrm{c1}} \\ \dfrac{({r_{\mathrm{c2}}}^2 - r^2)^2(2r^2 + {r_{\mathrm{c2}}}^2 - 3{r_{\mathrm{c1}}}^2)}{({r_{\mathrm{c2}}}^2 - {r_{\mathrm{c1}}}^2)^3} & r_{\mathrm{c1}} \le r \le r_{\mathrm{c2}} \\ 0 & r > r_{\mathrm{c2}} \end{cases} \tag{2}$$

where σ_{ij} and ε_{ij} are the size and energy parameters, respectively, and q_i denotes the value of the partial charge placed at the interaction site i. The interaction parameters are provided in Table 1. Cross-interaction parameters are computed using Lorentz−Berthelot combining rules.[36−38] $S(r)$ represents a switching function that brings the Lennard-Jones potential to zero between $r_{\mathrm{c1}} = 9.2$ Å and $r_{\mathrm{c2}} = 10$ Å. Electrostatic interactions are calculated using the Ewald sum method.[39]

Table 1. Potential Parameters for the Model Studied

model	atom	σ (Å)	ε (kJ mol^{-1})	q (e)
SPC/E[34]	O	3.166	0.650	−0.8476
	H	0	0	0.4238
TraPPE-UA[33]	CH_3	3.75	0.8149	0
	CH_2	3.95	0.3825	0
silica wall[35]	H	0	0	0.4
	O	3.154	0.6487	−0.71
	Si	3.795	0.5336	0.31

Simulation Details. Interfacial simulations are completed using a rectangular parallelepiped simulation box ($L_x = 34.58$, $L_y = 29.94$, and $L_z = 120$ Å) with periodic boundary conditions applied in the x and y directions. The system is closed at two ends of the nonperiodic z direction with the silica wall (34.58 × 29.94 × 14.95 Å) placed at the bottom of the box and a structureless "control" wall located at the other end. The substrate potential at the control wall is described by

$$u_{\mathrm{c}i}(z) = \begin{cases} \infty & z \le 0 \\ \varepsilon_{\mathrm{c}} S(z)\left[\left(\dfrac{\sigma_{\mathrm{c}}}{z}\right)^{9} + m_i\right] & 0 < z \le z_{\mathrm{c2}} \\ 0 & z > z_{\mathrm{c2}} \end{cases} \tag{3}$$

where z is the distance between a fluid interaction site and the wall. Here, the switching function $S(z)$ brings the potential to zero between $z_{\mathrm{c1}} = 0$ and $z_{\mathrm{c2}} = 4\sigma_{\mathrm{c}}$. For the water spreading method, we take m_i to be +1 for water and −1 for octane when constructing $W^{\mathrm{w,os}}(l^{\mathrm{w}})$. In this case, the control wall is setup to be repulsive to water ($m_{\mathrm{w}} = +1$) and attractive to octane ($m_{\mathrm{o}} = -1$). For the octane spreading method, we take m_i to be −1 for water and +1 for octane when constructing $W^{\mathrm{o,ws}}(l^{\mathrm{o}})$. The control wall is then repulsive to octane ($m_{\mathrm{o}} = +1$) and attractive to water ($m_{\mathrm{w}} = -1$). We use potential parameters $\sigma_{\mathrm{c}} = 4$ Å and $\varepsilon_{\mathrm{c}} = 4.157$ kJ mol^{-1}.

We reproduce the hydroxylated β-cristobalite (111) surface following the work of Lee and Rossky.[35] For this silica model, partial charges are placed on oxygen, silicon, and hydrogen atoms closest to the fluid interface (first layer only). The substrate is electrostatically neutral. The surface charges are used to control the polarity of the substrate. Specifically, we scale the charge of the surface Si, O, and H atoms by a constant k, with $q_i = kq_i^o (0 \leq k \leq 1)$, i= Si, O, H, and q_i^o is the partial charge value for the standard silica surface. Therefore, $k = 1$ corresponds to the fully hydroxylated substrate, and $k = 0$ maps to a nonpolar surface. Giovambattista et al.[9] characterize surfaces with $k < 0.4$ as hydrophobic and those with $k > 0.4$ as hydrophilic at $T = 300$ K.

Simulations are conducted within the grand canonical (GC) ensemble wherein the temperature T, activities ξ_i, and volume V are fixed. For convenience, we use the activity sum $\chi = \sum \xi_i$ and activity fraction $\eta_i = \xi_i/\chi$ to characterize the activities. The state condition $[T, \xi_i]$ is set to conditions corresponding to a bulk saturation point. The bulk saturation conditions for the water−octane mixture considered here were determined in an earlier study.[40] One set of calculations is performed at a liquid−liquid saturation point defined by $T = 400$ K, $\eta_o = 0.833$, and $\ln \chi = -8.923$. A second set of simulations is performed at a saturation point defined by $T = 300$ K, $\eta_o = 0.964$, and $\ln \chi = -11.746$. In both cases, the pressure evaluates to $p = 10$ MPa. The volume is characterized by the dimensions of the simulation box noted above.

The methods employed to sample the configurational space of the interfacial systems considered here are detailed in our previous papers.[22,40] Approximately 576 h of computational effort on six 2.40 GHz Intel Xeon E5645 processors with 12 cores was used to generate one water spreading potential $W^{w,os}(l^w)$ (see Figure 1).

Statistical uncertainties are determined by performing four independent sets of simulations. The standard deviation of the results from the four simulation sets is taken as an estimate of the statistical uncertainty.

RESULTS AND DISCUSSION

Wetting Properties. We begin by considering the water spreading interface potential for several substrate polarities at 400 K. These free energy curves provide insight regarding how the wetting behavior evolves with substrate hydrophilicity. Figure 1 contains $W^{w,os}$ at select surface polarities k from 0.4 to 1.0. The water molecule number is used as a measure of the thickness of the water film adjacent to the silica substrate. As a point of reference, a water molecule number of $N_w = 1200$ corresponds to a film thickness of $l^w \approx 38$ Å. For low k, we observe a global minimum in $W^{w,os}$ at $N_w \approx 0$, followed by a transition to a plateau region that develops around $N_w \approx 220$ ($l^w \approx 7$ Å). The difference between the minimum and plateau ($s^{w,os}$) is relatively large in magnitude, indicating that the system is well within the partial wetting regime. As the surface polarity increases beyond $k \approx 0.6$, the global minimum shifts to higher N_w. The shift in N_w stems from the adsorption of water at the silica−octane interface. The progressively stronger interaction between water and silica increases the driving force for water to adsorb at the interface. At the maximum surface polarity studied ($k = 1.0$), the global minimum in $W^{w,os}$ appears at $N_w \approx 55$. As discussed further below, this corresponds to a physical situation in which a monolayer of water adsorbs at the interface.

The interface potentials highlight another interesting aspect of the wetting behavior. For relatively low substrate polarity, the water spreading coefficient decreases in magnitude with increasing substrate polarity. In other words, the system tends toward the water wetting point. However, the magnitude of $s^{w,os}$ then reaches a minimum around $k \approx 0.8$, with further increases in substrate polarity resulting in an increase in the magnitude of $s^{w,os}$. Given that the water−octane interfacial tension remains constant along this path, this suggests that the water contact angle reaches a minimum upon variation of substrate polarity. The system initially approaches the wetting point, but at $k \approx 0.8$, the system then trends away from the wetting point with increasing substrate polarity.

To better understand how substrate polarity influences wetting properties, we complete a series of substrate polarity expanded ensemble simulations at temperatures of 300 and 400 K. These calculations enable us to trace the evolution of spreading coefficients with substrate polarity. Figure 2 provides $s^{w,os}$, $s^{o,ws}$, and γ^{ow} as a function of k. For reference, we note that as $s^{o,ws} \to 0$, the system approaches the octane wetting point, and as $s^{w,os} \to 0$, the system approaches the water wetting point. At relatively low k, the system exhibits the expected behavior. Over the range of $k \in [0,0.77]$ at 300 K and $k \in [0,0.84]$ at 400 K, the system evolves from near octane wetting conditions toward the water wetting point with increasing substrate polarity. From a physical perspective, the increase in substrate polarity strengthens the interaction between water and silica while having no impact on the strength of the interaction between octane and silica. One then expects the preference for the water-rich phase at the silica substrate to increase with increasing polarity and for the system to tend toward the water wetting point. Indeed, this trend is what we observe. However, at $k \approx 0.77$ at 300 K and at $k \approx 0.84$ at 400 K, the behavior qualitatively changes, with the system now driven away from the water wetting point with increasing substrate polarity. This change suggests a modification to the nature of the underlying silica−water interaction. Increasing k now appears to reduce the strength of this interaction. Finally, we note that γ^{ow} remains statistically constant upon variation of k. This trend is expected, as the substrate has no impact on the

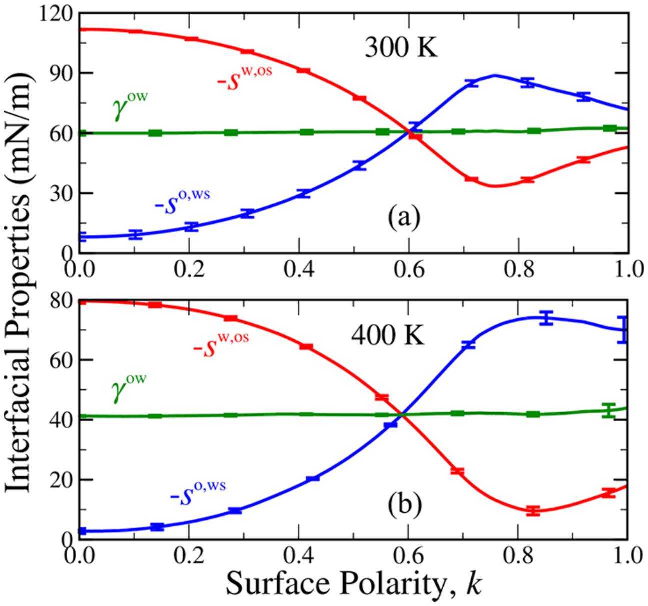

Figure 2. Evolution of the water spreading coefficient (solid red line), octane spreading coefficient (solid blue line), and octane−water interfacial tension (solid green line) at (a) 300 and (b) 400 K. Uncertainty estimates are provided at selected surface polarities.

water−octane interface, and serves as a consistency check for our calculations.

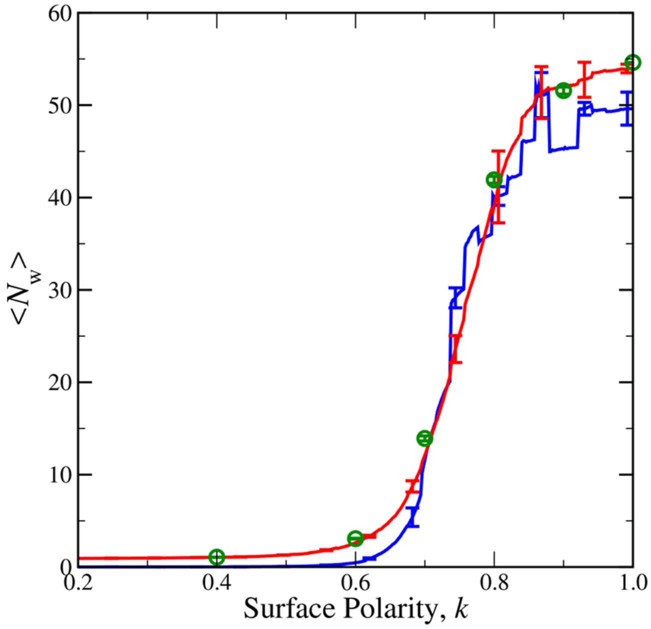

Figure 3. Evolution of the average number of water molecules associated with the minimum region of the water spreading interface potential with surface polarity. The solid blue and red curves represent results from expanded ensemble simulations at 300 and 400 K, respectively. Open green circles correspond to results from analysis of full water spreading interfacial potentials at 400 K.

We now examine the extent of water adsorption at the silica interface. Figure 3 provides the average number of water molecules within the simulation box as a function of substrate polarity. For direct simulations in which we capture $W^{\mathrm{w,os}}(N_\mathrm{w})$, the free energy curve is translated to a probability distribution $\Pi(N_\mathrm{w}) \sim \exp[-W^{\mathrm{w,os}}(N_\mathrm{w})/kT]$, and we evaluate the ensemble average in the usual manner $\langle N_\mathrm{w}\rangle = \sum N_\mathrm{w}\Pi(N_\mathrm{w})$. For expanded ensemble simulations, one of the two independent calculations used to trace $s^{\mathrm{w,os}}$ follows the minimum region of the interface potential. Within these simulations, we capture $\Pi(N_\mathrm{w})$ within each subensemble using a visited state approach and evaluate the ensemble average via $\langle N_\mathrm{w}\rangle = \sum N_\mathrm{w}\Pi(N_\mathrm{w})$. At relatively low k, $\langle N_\mathrm{w}\rangle$ evaluates to a value consistent with the temperature-specific concentration of water within the octane-rich fluid phase. In other words, the surface density of water is negligible. For both temperatures studied, we observe a rapid increase in $\langle N_\mathrm{w}\rangle$ at $k \approx 0.6$. This rapid increase persists until $k \approx 0.85$ at which points the value of $\langle N_\mathrm{w}\rangle$ remains relatively constant at $\langle N_\mathrm{w}\rangle \approx 50$. As is detailed further below, this value closely aligns with the number of water molecules needed to form a monolayer of water on the β-cristobalite (111) surface.

The evolution of the cosine of the contact angle with substrate polarity is shown in Figure 4. The cos θ curve reaches a maximum at $k = 0.76$ ($\theta = 63°$) for 300 K and at $k = 0.84$ ($\theta = 40°$) for 400 K. Beyond the maximum, the degree of water adsorption at the silica−octane interface is enhanced significantly. This enhanced water adsorption is consistent with a physical scenario in which the water droplet sits atop a monolayer-thick precursor film that surrounds the droplet. At relatively low k, the traditional wetting scenario of an isolated droplet persists. We note that the contact angle evaluates to $\theta = 90°$ at $k = 0.59$, a traditional point for delineating between a hydrophobic and hydrophilic surface.

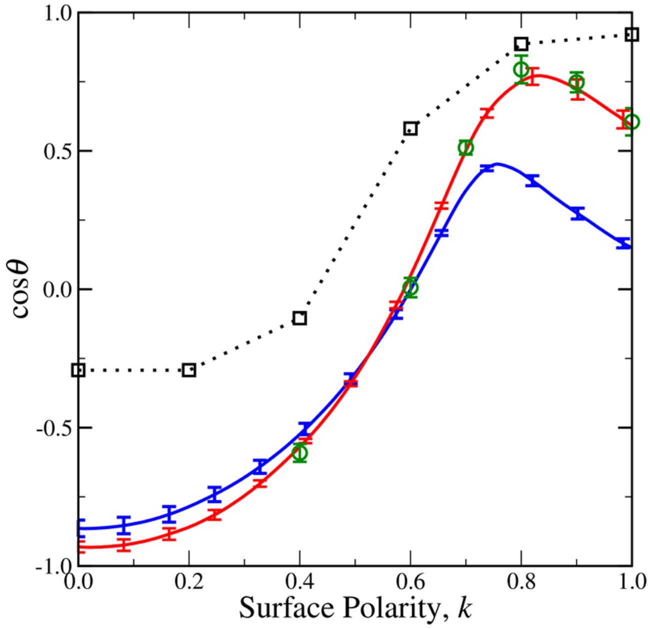

Figure 4. Evolution of the water contact angle with surface polarity. Symbols are identical to those in Figure 3. The additional open black squares represent data from Giovambattista et al.[9] for the contact angle of a water droplet in a vapor background. The black dotted line simply connects the data points from Giovambattista et al.[9]

We also include in Figure 4 the evolution of cosθ with k captured by Giovambattista et al.[9] Recall that this group examined the wetting properties of a system consisting of water only at the same silica substrate. The mother background phase in the work of Giovambattista et al. is water vapor, whereas liquid octane plays this role in the current study. In general, changing the mother background phase from water vapor to a hydrocarbon liquid reduces the water wettability (cosθ decreases). This result is physically reasonable. The introduction of an immiscible liquid creates a scenario in which both liquids compete to locate in the vicinity of the substrate. Interestingly, the Giovambattista et al. data for cosθ do not exhibit a maximum upon variation of k. However, the change in cosθ with k slows as the system approaches the wetting point.

Structure of Water at Silica Surface. We now study the manner in which water organizes at the silica substrate. We consider two conditions. The first corresponds to conditions at the minimum in the water spreading interface potential, and the second corresponds to the plateau region of the interface potential. For the first condition, we observe negligible water density at low k and a monolayer of water at relatively high k. Therefore, we often refer to this set of configurations as the "monolayer" case. The second condition is associated with a relatively thick water film adjacent to the silica substrate. We often refer to this set of configurations as the "film" case. We consider configurations generated at 400 K to complete the structural analysis.

Figure 5 contains a representative snapshot of the water monolayer associated with the minimum in $W^{\mathrm{w,os}}(l^\mathrm{w})$ for the $k = 1.0$ substrate. We observe that water molecules preferentially sit at regular positions defined by the topography of the β-

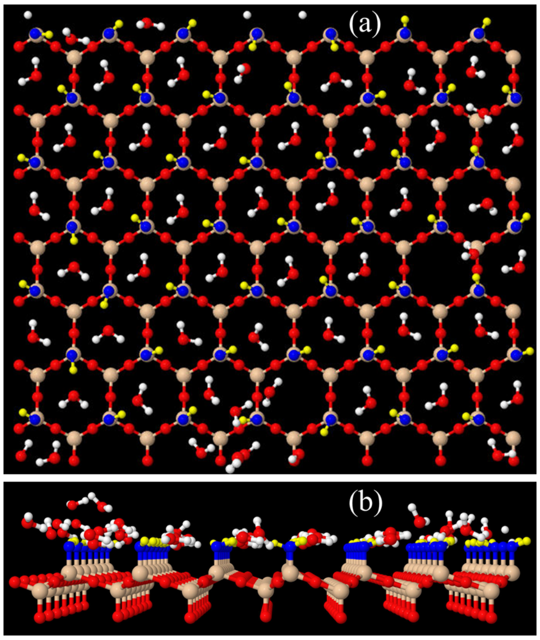

Figure 5. (a) Top and (b) side views of a water monolayer configuration. Silicon (brown), oxygen in the first layer of silica (blue), oxygen otherwise (red), hydrogen in water (white), and hydrogen in silica (yellow) atoms are displayed.

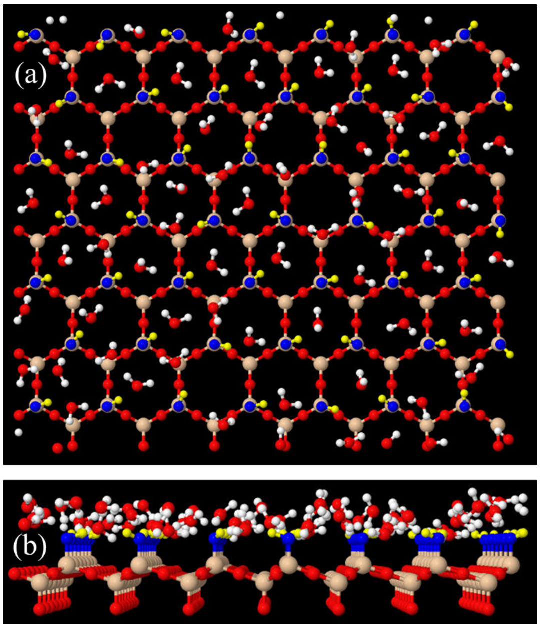

Figure 6. (a) Top and (b) side views of a water film configuration. We include water molecules that reside within 4 Å of the silicon atoms within the first layer of the substrate. Atoms are colored as described in Figure 5.

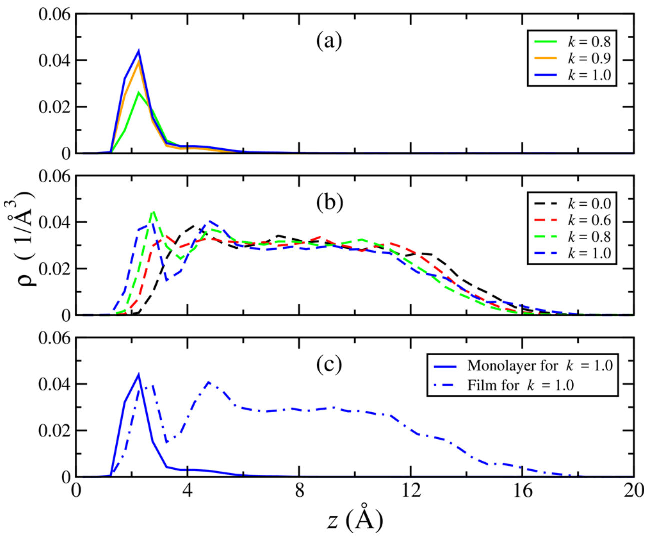

Figure 7. Oxygen atom density profile for (a) water monolayer with k = 0.8, 0.9, and 1.0, (b) water film with k = 0.0 0.6, 0.8, and 1.0, and (c) monolayer and film with k = 1.0. Line styles are defined within the legends.

cristobalite (111) surface. More specifically, water molecules tend to sit within the hollows of the substrate, near the center point of triangles formed by three neighboring silanol groups. The hydrogen atoms of a given water molecule point toward two of the silanol oxygen atoms, and the hydrogen atom within a silanol group points toward the lone pair electrons of the water molecule. The structure observed is consistent with the pattern identified by Yang et al. via density functional theory.[26] Here, the perfect pattern reported by Yang et al. is broken at nonzero temperature, but the underlying structure is evident.

Figure 6 contains a representative snapshot of water molecules that reside within a water film at the k = 1.0 substrate. We focus on the first hydration layer, defined as water that resides within 4 Å of the silicon atoms within the first layer of the substrate. We observe the same underlying pattern as for the monolayer. However, the water is less structured at conditions that correspond to the plateau region (thick film) of the interface potential relative to the minimum (monolayer). Within the relatively thick water film, water at the silica interface forms hydrogen bonds with both the silica substrate and the adjacent water film. In contrast, water in the monolayer primarily forms hydrogen bonds with the silica substrate. It follows that the monolayer structure is more aligned with the topography of the substrate. We provide quantitative evidence for this observation below. Finally, we note that a similar analysis of n-octane at the silica substrate did not reveal preferential ordering of the fluid with respect to the substrate topography.

Figure 7 provides the oxygen density profile for the monolayer (Figure 7a) and film (Figure 7b) for various substrate polarities. The z = 0.0 point is defined by the location of the silicon atoms within the first layer of the substrate. The local density is partitioned into slabs with a width of 0.5 Å. In general, the fluid is drawn closer to the substrate as the polarity increases. This observation is consistent with the evolution of the fluid structure with the strength of the substrate−fluid interaction reported in earlier studies.[9] The density profile for the monolayer is consistent with a single layer of the adsorbed fluid; the local water density is negligible beyond $z \approx 3.5$ Å. For water films at substrates with $k \geq 0.6$, we observe an initial peak at $z \approx 2.8$ Å and a second peak at $z \approx 4.7$ Å. The distinction between the two peaks increases with increasing polarity. At relatively high polarity, the demarcation between the two peaks is rather clear, suggesting that water in the first two layers of the film organizes in a distinct manner. The fluid structure at the hydrophobic substrate (k = 0.0) is qualitatively different. The fluid is relatively depleted from the substrate, with the emergence of the initial peak in the density profile

DOI: 10.1021/acs.jpcc.9b04970
J. Phys. Chem. C 2019, 123, 19649−19658

delayed to $z \approx 4$ Å. Finally, at a position of $z \approx 8$ Å, the oxygen density reaches a value that is consistent with the bulk liquid.

Figure 7c provides a comparison of the monolayer and film density profiles for the $k = 1.0$ substrate. A first peak emerges at positions of $z = 2.25$ Å and $z = 2.75$ Å for the monolayer and film, respectively. This result indicates that water molecules reside deeper within the substrate hollows for the monolayer than for the film. Water molecules shift away from the substrate as the water film thickness increases. This difference is likely due to the competition between water−silica and water−water interactions within the film. By shifting to slightly higher positions, water molecules within the hollows are able to form stronger hydrogen bonds with water molecules in the adjacent film.

We next examine the radial distribution functions (RDFs) for interfacial water at substrates of varying polarity. Figure 8a shows the oxygen−oxygen radial distribution function $g_{\mathrm{OO}}(r)$ of monolayer water at $k = 0.8, 0.9, 1.0$. For $g_{\mathrm{OO}}(r)$, a first peak is observed at a separation distance of 2.8 Å, and a second peak appears at 5.1 Å. The first peak is consistent with that observed for bulk water and is associated with water−water hydrogen bonding. The location of the second peak is consistent with the separation distance (4.94 Å) of neighboring unit cells within the β-cristobalite (111) surface. The emergence of this peak is consistent with water molecules residing within the hollows of the substrate. As the substrate polarity increases, the density of the first peak decreases, and that of the second peak increases. As a result of the stronger interaction between the substrate and water molecules, water molecules preferentially move to the substrate hollows wherein they form three in-plane hydrogen bonds with neighboring silanol groups. Water molecules are then less likely to hydrogen bond with neighboring water molecules.

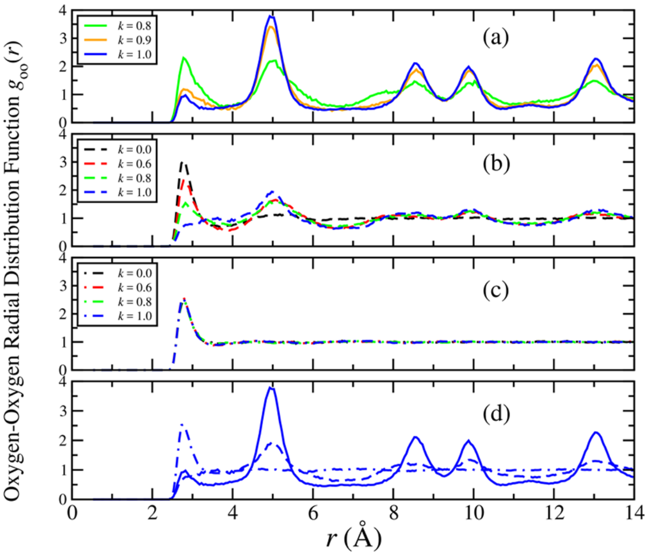

Figure 8. Oxygen−oxygen radial distribution functions for (a) water monolayer with $k = 0.8$, 0.9, and 1.0, (b) first layer of water film with $k = 0.0$ 0.6, 0.8, and 1.0, (c) second layer of water film with $k = 0.0$ 0.6, 0.8, and 1.0, and (d) monolayer, first layer of film, and second layer of film with $k = 1.0$. Solid, dashed, and dot-dashed lines are used to represent the water monolayer, first layer of water film, and second layer of water film, respectively. The $k = 0.0$, 0.6, 0.8, 0.9, and 1.0 cases are represented by black, red, green, orange, and blue curves.

Figure 8b,c shows $g_{\mathrm{OO}}(r)$ for water within the first and second hydration layer of the film, respectively, at various substrate polarities. The first two layers are defined by z from 2 to 4 Å and 4 to 6 Å. The $g_{\mathrm{OO}}(r)$ curves for water within the first hydration layer of the film at substrates with $k \geq 0.6$ show the same qualitative trends as observed for the monolayer. As the substrate polarity increases, the peak associated with water−water hydrogen bonding decreases in amplitude, while the peak associated with water in the substrate hollows increases in prominence. The $g_{\mathrm{OO}}(r)$ curve for the hydrophobic substrate ($k = 0.0$) is similar to that for bulk water. The hydrophobic substrate appears to have a relatively little impact on how water organizes in the vicinity of the surface. The pair correlation functions for the second layer of the film collapse onto a nearly common curve over the range of substrate polarities studied. Moreover, the near common $g_{\mathrm{OO}}(r)$ is consistent with that of bulk water. This result suggests that the length scales over which the substrate influences the manner in which water organizes do not extend significantly beyond the first layer. Figure 8d provides a comparison of $g_{\mathrm{OO}}(r)$ for water within the first film layer, second film layer, and monolayer for the $k = 1.0$ substrate. The peaks for the first film layer are less pronounced than those for the monolayer, indicating a lower level of the in-plane order within the film. This shift is consistent with visual inspection of configurational snapshots from the monolayer and film.

It is clear that silica substrates with high polarity strongly influence the manner in which water organizes at the interface. To better understand how water molecules orient at the interface, we calculate probability distributions for the angles ϕ_μ, ϕ_{OH}, ψ_μ, and ψ_{OH}. Here, ϕ_μ is defined as the angle between the water dipole vector $\vec{\mu}$ and the unit vector normal to the surface pointing into the water film. ϕ_{OH} is the angle between the unit normal and the $\overrightarrow{\mathrm{OH}}$ vector pointing from a water oxygen to a water hydrogen. There are two such angles per water molecule. ψ_μ is defined as the angle between the dipole moment vector and the x axis, and ψ_{OH} represents the angle between an $\overrightarrow{\mathrm{OH}}$ vector and the x axis.

Figures 9 and 10 provide probability distributions related to ϕ_{OH} and ϕ_μ, respectively. The distribution $P(\cos\phi)$ is uniform for a randomly distributed system, and therefore, we work with this quantity. Figures 9a and 10a provide distributions for the monolayer. The $\cos\phi_{\mathrm{OH}}$ distributions show a primary peak at $\phi_{\mathrm{OH}} \approx 90°$ and a secondary peak at $\phi_{\mathrm{OH}} \approx 0°$. The first peak corresponds to $\overrightarrow{\mathrm{OH}}$ vectors that orient parallel to the substrate. Such an orientation is consistent with water residing in the substrate hollows and forming hydrogen bonds with silanol groups. The secondary peak is representative of $\overrightarrow{\mathrm{OH}}$ vectors that point into the bulk fluid, potentially forming hydrogen bonds with water molecules that reside above the substrate. The $\cos\phi_\mu$ distributions show a peak at $\phi_\mu \approx 80°$, suggesting that the dipole vectors orient slightly out of the plane parallel to the substrate, pointing toward the bulk fluid. The distributions become sharper as the polarity of the substrate increases, indicating that the monolayer molecules orient in a more planar manner as the polarity increases.

Figures 9b and 10b show $\cos\phi_{\mathrm{OH}}$ and $\cos\phi_\mu$ distributions for the first hydration layer of the film. The $k = 0.8$ and 1.0 $\cos\phi_{\mathrm{OH}}$ distributions are relatively structured with peaks at $\phi_{\mathrm{OH}} \to 0°$ and $\phi_{\mathrm{OH}} \approx 110°$. These peak locations are consistent with water molecules that sit slightly above the substrate with one

DOI: 10.1021/acs.jpcc.9b04970
J. Phys. Chem. C 2019, 123, 19649−19658

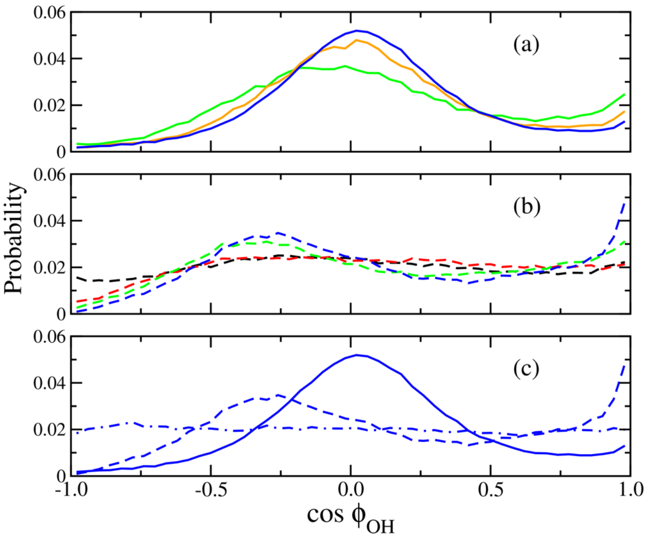

Figure 9. ϕ_{OH} probability distributions for (a) water monolayer with k = 0.8, 0.9, and 1.0, (b) first layer of water film with k = 0.0 0.6, 0.8, and 1.0, and (c) monolayer, first layer of film, and second layer of film with k = 1.0. Lines styles are identical to those defined in Figure 8.

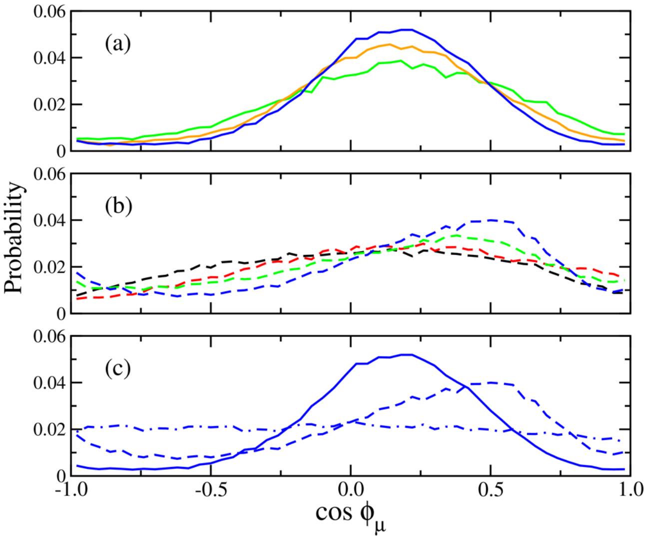

Figure 10. ϕ_μ probability distributions for (a) water monolayer with k = 0.8, 0.9, and 1.0, (b) first layer of water film with k = 0.0 0.6, 0.8, and 1.0, and (c) monolayer, first layer of film, and second layer of film with k = 1.0. Lines styles are identical to those defined in Figure 8.

hydrogen oriented moderately out-of-plane pointing toward the substrate and another oriented perpendicular to the substrate pointing toward the bulk fluid. In contrast, the k = 0.6 distribution is relatively flat after cos$\phi_{OH} > -0.5$, suggesting a relatively little orientational preference within this region. We also observe that $P(\cos\,\phi_{OH}) \to 0$ as cos$\phi_{OH} \to -1$ for substrates with $k \geq 0.6$, indicating that water is unlikely to orient with the $\overrightarrow{\mathrm{OH}}$ vector pointing into substrates that are relatively hydrophilic. The cosϕ_{OH} distribution is relatively uniform for the hydrophobic substrate (k = 0.0), which again supports the notion that this substrate has relatively little influence on the manner in which interfacial water organizes. The cosϕ_μ distributions for weak surfaces are relatively broad and centered around $\phi_\mu \approx 90°$ (in-plane orientation). As the polarity increases, the dipole vector preferentially moves to lower angles $\phi_\mu \approx 60°$ and shows an enhanced preference for pointing into the substrate $\phi_\mu \to 180°$. The former position of the dipole vector is consistent with the water orientation noted just above.

Figures 9c and 10c provide a comparison of these distributions for the first film layer, second film layer, and monolayer for the k = 1.0 substrate. Water within the first layer of the film and within the monolayer again exhibits qualitatively similar structural patterns. The $P(\cos\,\phi_{OH})$ peak associated with $\overrightarrow{\mathrm{OH}}$ vectors oriented in the plane parallel to the surface shifts from $\phi_{OH} \approx 90°$ for the monolayer to $\phi_{OH} \approx 110°$ for the first layer of the film. In contrast, the analogous peak in the $P(\cos\,\phi_\mu)$ distribution shifts from $\phi_\mu \approx 80°$ for the monolayer to $\phi_\mu \approx 60°$ for the first layer of the film. We also observe that the first-layer film peak associated with $\overrightarrow{\mathrm{OH}}$ vectors oriented perpendicular to the substrate is more pronounced relative to the monolayer case. In addition, the likelihood of the dipole moment vector pointing into the substrate ($\phi_\mu \approx 180°$) is enhanced in the first layer of the film relative to the monolayer. Collectively, these shifts are consistent with water in the first layer of the film adopting slightly higher positions relative to the monolayer and forming hydrogen bonds between first- and second-layer water molecules. Water−water hydrogen bonds of this type are rare in the monolayer case. Finally, we note that the $P(\cos\,\phi)$ distributions for water in the second layer of the film are nearly uniform, indicating that the substrate has relatively little influence on the water structure in this region of the film.

Figures 11 and 12 provide probability distributions related to ψ_{OH} and ψ_μ, respectively. The system is symmetric with respect to the x axis, and therefore, we consider $|\cos\,\psi_{OH}|$ and $|\cos\,\psi_\mu|$ distributions for water molecules in the monolayer. Figures 11a and 12a contain distributions for the monolayer. The $|\cos\,\psi_{OH}|$ distribution exhibits peaks at $|\cos\,\psi_{OH}| \approx 0.0$ and 0.9, which corresponds to three preferred ψ_{OH} angles of 90°, 26°, and 154°. The $|\cos\,\psi_\mu|$ distribution exhibits a pronounced peak at $|\cos\,\psi_\mu| \approx 0.86$, which corresponds to preferred ψ_μ

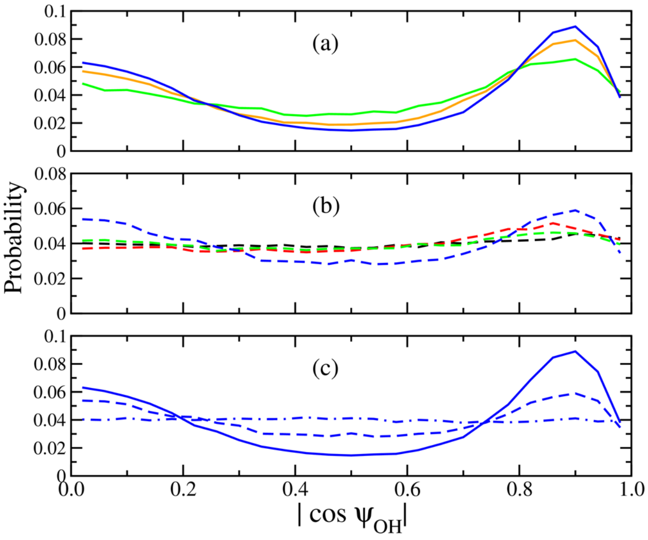

Figure 11. ψ_{OH} probability distributions for (a) water monolayer with k = 0.8, 0.9, and 1.0, (b) first layer of water film with k = 0.0 0.6, 0.8, and 1.0, and (c) monolayer, first layer of film, and second layer of film with k = 1.0. Lines styles are identical to those defined in Figure 8.

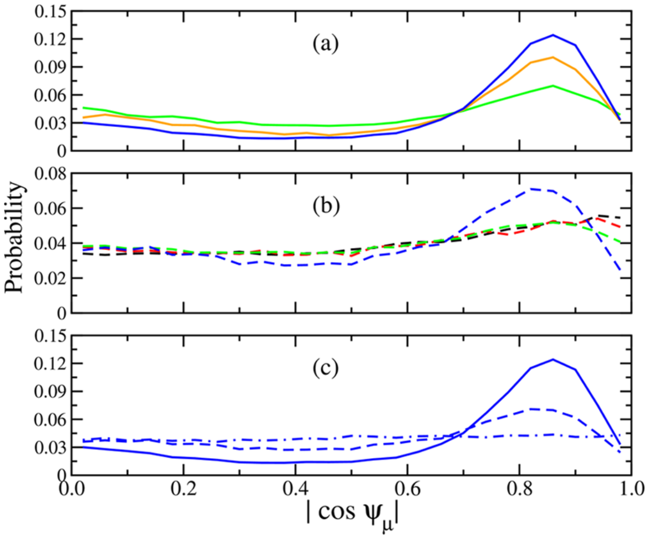

Figure 12. ψ_μ probability distributions for (a) water monolayer with k = 0.8, 0.9, and 1.0, (b) first layer of water film with k = 0.0 0.6, 0.8, and 1.0, and (c) monolayer, first layer of film, and second layer of film with k = 1.0. Lines styles are identical to those defined in Figure 8.

angles of 30° and 150°. The results suggest three preferred orientations for water molecules in the plane parallel to the substrate. The distributions are consistent with water molecules forming three hydrogen bonds with substrate silanol groups. Again, the distributions become sharper as the polarity of the substrate increases.

Figures 11b and 12b contain distributions for the first hydration layer of the water film. The hydrophobic substrate shows a relatively little preference with respect to the ψ_{OH} angle. However, as the polarity of the system increases, the system shows increasing preference for ψ_{OH} angles of 90°, 26°, and 154°. In a similar manner, the system shows increasing preference for ψ_μ angles of 30° and 150° as the polarity increases. Figures 11c and 12c provide a comparison of the ψ_{OH} and ψ_μ distributions for the first film layer, second film layer, and monolayer for the k = 1.0 substrate. We again observe that the first film layer and monolayer share qualitatively similar patterns. The positions of the first film layer and monolayer peaks are consistent, but the amplitudes of the peaks for the monolayer are more pronounced. The distributions suggest three preferred orientations within the plane parallel to the substrate. These orientations align with the topography of the underlying lattice.

■ CONCLUSIONS

We used molecular simulation to investigate how substrate polarity influences the wetting and structural properties of water at the β-cristobalite (111) surface in a mother hydrocarbon liquid. Complete water spreading interface potentials were obtained at select substrate polarities. In addition, expanded ensemble methods were employed to carefully track the variation of wetting properties with substrate polarity at temperatures of 300 and 400 K. Various metrics were computed to characterize the structure of water at the interface. These included the water density profile, in-plane oxygen−oxygen radial distribution function, and four angles that capture the orientation of the water oxygen−hydrogen bond vector and dipole moment vector relative to the substrate normal and within the plane parallel to the substrate.

Our results highlight an anomalous trend in the contact angle of water. The contact angle exhibits a nonmonotonic response upon variation of the substrate polarity. Upon increasing the polarity from hydrophobic conditions, the system initially tends toward the water wetting point, as is expected. However, at a sufficiently high value of the polarity, the contact angle exhibits a minimum, and further increases in polarity lead to an increase in the contact angle. Around this extremum point, the surface density of water changes rapidly, with a monolayer of water assembling on the substrate at relatively high substrate polarity. Prior to the minimum (low polarity), the water droplet sits on a silica substrate that is void of water beyond of the droplet perimeter. After the minimum (high polarity), the water droplet is surrounded by a monolayer-thick precursor film.

Reviewing structural information enabled us to link the onset of the precursor film to the manner in which water organizes at the substrate. When the silica−water interaction becomes sufficiently strong, water molecules preferentially reside within the hollows associated with the topography of the β-cristobalite (111) surface. More specifically, water molecules tend to sit near the center point of triangles defined by three silanol groups. This configuration facilitates the formation of three hydrogen bonds within the plane parallel to the substrate. The development of the monolayer leads to the formation of an effective composite substrate consisting of silica and a monolayer of water. As the substrate polarity increases, the monolayer molecules progressively orient in a more planar manner, thus reducing opportunities for bulk water to hydrogen bond with water within the monolayer. Water molecules beyond the first layer are not significantly influenced by variation of the substrate polarity. As a result, once the polarity is sufficiently high, further increases effectively weaken the substrate−water interaction. From a macroscopic perspective, the weaker interaction results in a larger water contact angle.

From a broad perspective, the system studied here provides an example of a case wherein the topography of the substrate, and the associated manner in which the fluid organizes at the interface governs the wetting behavior. In other words, simple metrics related to the scalar strength of the underlying surface-fluid interaction do not accurately forecast the evolution of the wetting properties. Minerals often present complex topographies and a mix of nonpolar and electrostatic interactions. Therefore, mineral systems are primary candidates for exhibiting anomalous wetting behavior. The results presented here show how molecular simulation can be used to map trends in macroscopic interfacial properties to the microscopic fluid structure at the interface. Further studies of the wetting behavior of water at mineral substrates would help provide a more robust understanding of the connection between substrate characteristics and water wetting behavior.

■ AUTHOR INFORMATION

Corresponding Author

*E-mail: jerring@buffalo.edu. Phone: +1 (716) 645-1184.

ORCID

Jeffrey R. Errington: 0000-0003-0365-0271

Notes

The authors declare no competing financial interest.

■ ACKNOWLEDGMENTS

We gratefully acknowledge the financial support of the National Science Foundation (grant no. CBET-1705620). Computational resources were provided in part by the University at Buffalo Center for Computational Research.

■ REFERENCES

(1) Morrow, N. R. Wettability and Its Effect on Oil Recovery. *J. Pet. Technol.* **2013**, *42*, 1476−1484.

(2) Kowalewski, E.; Holt, T.; Torsaeter, O. Wettability Alterations Due to an Oil Soluble Additive. *J. Pet. Sci. Eng.* **2002**, *33*, 19−28.

(3) Hirasaki, G. J. Application of the Theory of Multicomponent, Multiphase Displacement to Three-Component, Two-Phase Surfactant Flooding. *Soc. Pet. Eng. J.* **2013**, *21*, 191−204.

(4) Grzelak, E. M.; Errington, J. R. Computation of Interfacial Properties Via Grand Canonical Transition Matrix Monte Carlo Simulation. *J. Chem. Phys.* **2008**, *128*, No. 014710.

(5) Sellers, M. S.; Errington, J. R. Influence of Substrate Strength on Wetting Behavior. *J. Phys. Chem. C* **2008**, *112*, 12905−12913.

(6) Rane, K. S.; Kumar, V.; Errington, J. R. Monte Carlo Simulation Methods for Computing the Wetting and Drying Properties of Model Systems. *J. Chem. Phys.* **2011**, *135*, 234102.

(7) Kumar, V.; Errington, J. R. Application of the Interface Potential Approach to Calculate the Wetting Properties of a Water Model System. *Mol. Simul.* **2013**, *39*, 1143−1152.

(8) Kumar, V.; Errington, J. R. Wetting Behavior of Water near Nonpolar Surfaces. *J. Phys. Chem. C* **2013**, *117*, 23017−23026.

(9) Giovambattista, N.; Debenedetti, P. G.; Rossky, P. J. Effect of Surface Polarity on Water Contact Angle and Interfacial Hydration Structure. *J. Phys. Chem. B* **2007**, *111*, 9581−9587.

(10) Phan, A.; Ho, T. A.; Cole, D. R.; Striolo, A. Molecular Structure and Dynamics in Thin Water Films at Metal Oxide Surfaces: Magnesium, Aluminum, and Silicon Oxide Surfaces. *J. Phys. Chem. C* **2012**, *116*, 15962−15973.

(11) Ho, T. A.; Argyris, D.; Papavassiliou, D. V.; Striolo, A.; Lee, L. L.; Cole, D. R. Interfacial Water on Crystalline Silica: A Comparative Molecular Dynamics Simulation Study. *Mol. Simul.* **2011**, *37*, 172−195.

(12) Argyris, D.; Ho, T.; Cole, D. R.; Striolo, A. Molecular Dynamics Studies of Interfacial Water at the Alumina Surface. *J. Phys. Chem. C* **2011**, *115*, 2038−2046.

(13) Shi, B.; Dhir, V. K. Molecular Dynamics Simulation of the Contact Angle of Liquids on Solid Surfaces. *J. Chem. Phys.* **2009**, *130*, No. 034705.

(14) Do Hong, S.; Ha, M. Y.; Balachandar, S. Static and Dynamic Contact Angles of Water Droplet on a Solid Surface Using Molecular Dynamics Simulation. *J. Colloid Interface. Sci.* **2009**, *339*, 187−195.

(15) Nijmeijer, M. J. P.; Bruin, C.; Bakker, A. F.; Van Leeuwen, J. M. J. A Visual Measurement of Contact Angles in a Molecular-Dynamics Simulation. *Phys. A* **1989**, *160*, 166−180.

(16) Saville, G. Computer Simulation of the Liquid-Solid-Vapour Contact Angle. *J. Chem. Soc., Faraday Trans. 2* **1977**, *73*, 1122−1132.

(17) Werder, T.; Walther, J. H.; Jaffe, R. L.; Halicioglu, T.; Koumoutsakos, P. On the Water−Carbon Interaction for Use in Molecular Dynamics Simulations of Graphite and Carbon Nanotubes. *J. Phys. Chem. B* **2003**, *107*, 1345−1352.

(18) MacDowell, L. G. Computer Simulation of Interface Potentials: Towards a First Principle Description of Complex Interfaces? *Eur. Phys. J.-Spec. Top.* **2011**, *197*, 131−145.

(19) MacDowell, L. G.; Müller, M. Observation of Autophobic Dewetting on Polymer Brushes from Computer Simulation. *J. Phys.: Condens. Matter* **2005**, *17*, S3523−S3528.

(20) Kumar, V.; Errington, J. R. Understanding Wetting of Immiscible Liquids near a Solid Surface Using Molecular Simulation. *J. Chem. Phys.* **2013**, *139*, No. 064110.

(21) Kumar, V.; Errington, J. R. Monte Carlo Simulation Strategies to Compute Interfacial and Bulk Properties of Binary Fluid Mixtures. *J. Chem. Phys.* **2013**, *138*, 174112.

(22) Guo, W.; Errington, J. R. Monte Carlo Simulation Strategies to Compute the Interfacial Properties of a Model Octane−Water−Silica System. *J. Phys. Chem. C* **2018**, *122*, 17309−17318.

(23) Guo, W.; Errington, J. R. Effect of Carboxylic Acid on the Wetting Properties of a Model Water−Octane−Silica System. *Langmuir* **2019**, *35*, 6540−6549.

(24) Hu, X. L.; Michaelides, A. Water on the Hydroxylated (001) Surface of Kaolinite: From Monomer Adsorption to a Flat 2d Wetting Layer. *Surf. Sci.* **2008**, *602*, 960−974.

(25) Puibasset, J.; Pellenq, R. J. M. Water Adsorption on Hydrophilic Mesoporous and Plane Silica Substrates: A Grand Canonical Monte Carlo Simulation Study. *J. Chem. Phys.* **2003**, *118*, 5613−5622.

(26) Yang, J.; Meng, S.; Xu, L.; Wang, E. G. Water Adsorption on Hydroxylated Silica Surfaces Studied Using the Density Functional Theory. *Phys. Rev. B* **2005**, *71*, No. 035413.

(27) Indekeu, J. O. Line Tension at Wetting. *Int. J. Mod Phys. B* **1994**, *08*, 309−345.

(28) de Gennes, P. G. Wetting: Statics and Dynamics. *Rev. Mod. Phys.* **1985**, *57*, 827−863.

(29) Dietrich, S. Wetting Phenomena. In *Phase Transitions and Critical Phenomena*; Domb, C.; Lebowitz, J. L., Eds.; Academic Press: London, 1988; Vol. *12*.

(30) Grzelak, E. M.; Errington, J. R. Calculation of Interfacial Properties Via Free-Energy-Based Molecular Simulation: The Influence of System Size. *J. Chem. Phys.* **2010**, *132*, 224702.

(31) Lyubartsev, A. P.; Martsinovski, A. A.; Shevkunov, S. V.; Vorontsov-Velyaminov, P. N. New Approach to Monte Carlo Calculation of the Free Energy: Method of Expanded Ensembles. *J. Chem. Phys.* **1992**, *96*, 1776−1783.

(32) Rane, K. S.; Murali, S.; Errington, J. R. Monte Carlo Simulation Methods for Computing Liquid−Vapor Saturation Properties of Model Systems. *J. Chem. Theory Comput.* **2013**, *9*, 2552−2566.

(33) Martin, M. G.; Siepmann, J. I. Transferable Potentials for Phase Equilibria. 1. United-Atom Description ofn-Alkanes. *J. Phys. Chem. B* **1998**, *102*, 2569−2577.

(34) Berendsen, H. J. C.; Grigera, J. R.; Straatsma, T. P. The Missing Term in Effective Pair Potentials. *J. Phys. Chem.* **1987**, *91*, 6269−6271.

(35) Lee, S. H.; Rossky, P. J. A Comparison of the Structure and Dynamics of Liquid Water at Hydrophobic and Hydrophilic Surfaces—a Molecular Dynamics Simulation Study. *J. Chem. Phys.* **1994**, *100*, 3334−3345.

(36) Allen, M. P.; Tildesley, D. *Computer Simulation of Liquids*; Clarendon Press: Oxford, U.K., 1989.

(37) Berthelot, D. Sur Le Mélange Des Gaz. *CR. Hebd. Acad. Sci.* **1898**, *126*, 1703−1855.

(38) Lorentz, H. A. Ueber Die Anwendung Des Satzes Vom Virial in Der Kinetischen Theorie Der Gase. *Ann. Phys.* **1881**, *248*, 127−136.

(39) Frenkel, D.; Smit, B. *Understanding Molecular Simulation*, 2nd ed.; Academic Press: San Diego, CA, 2002.

(40) Guo, W.; Bali, P.; Errington, J. R. Calculation of the Saturation Properties of a Model Octane−Water System Using Monte Carlo Simulation. *J. Phys. Chem. B* **2018**, *122*, 6260−6271.

DOI: 10.1021/acs.jpcc.9b04970
J. Phys. Chem. C 2019, 123, 19649−19658